Technical Note	LIGO-T2200205–v1	2022/07/29

Developing an In-Air IR Test Facility for Next-Generation Wavefront Control

Cassidy Nicks

California Institute of Technology
LIGO Project, MS 18-34
Pasadena, CA 91125
Phone (626) 395-2129
Fax (626) 304-9834
E-mail: info@ligo.caltech.edu

Massachusetts Institute of Technology
LIGO Project, Room NW22-295
Cambridge, MA 02139
Phone (617) 253-4824
Fax (617) 253-7014
E-mail: info@ligo.mit.edu

LIGO Hanford Observatory
Route 10, Mile Marker 2
Richland, WA 99352
Phone (509) 372-8106
Fax (509) 372-8137
E-mail: info@ligo.caltech.edu

LIGO Livingston Observatory
19100 LIGO Lane
Livingston, LA 70754
Phone (225) 686-3100
Fax (225) 686-7189
E-mail: info@ligo.caltech.edu

http://www.ligo.caltech.edu/

1 Abstract

Thermally-induced defects, particularly point absorbers, are a persistent problem in ramping up LIGO's power to lower the quantum noise floor (the sensing limit imposed by photon shot noise). One proposed solution is to use a ring heater adaptive optics device to project a thermal correction map onto the LIGO test masses to minimize the scattering into higher order mode. In order to test this concept, an in-air IR test facility, with a focus on the control of the IR camera, is developed. Using an IR-absorptive thin screen with an IR camera behind it, the thermal maps created by the ring heater can be tested and refined. By developing code to control the camera, particularly fine-tuning control over temperature measurements, these thermal maps and their effectiveness can be accurately analyzed.

2 Introduction

In 1893, gravitational waves were first proposed by Oliver Heaviside when noting the similarities between the inverse square laws of electrical charges and gravity; a little over a decade later, Henri Poincaré proposed that these possible waves would have to move at the speed of light [1, 2]. However, it was not until Einstein's Theory of General Relativity in 1916 that gravitational waves were predicted by a physical model [3]. In essence, gravitational waves can be described as ripples in spacetime caused by accelerating massive objects. The strongest, and thus most measurable, gravitational waves are caused by huge astronomical events like colliding black holes and neutron stars, as well as supernovae. Unlike electromagnetic radiation, gravitational waves only weakly interact with matter between source and detection, making them invaluable tools for understanding the mechanisms of their sources. After Einstein's predictions, however, the existence of gravitational waves was hotly debated, even by Einstein himself. It took until 2015 for gravitational waves, caused by two colliding black holes, to be directly detected at aLIGO (advanced Laser Interferometer Gravitational-wave Observatory).

aLIGO's construction, building on the initial LIGO model, began in 2008. LIGO is essentially a set of two massive Michelson interferometers, one in Louisiana and one in Washington, with 4 km long perpendicular arms that form an L-shape (see Figure 1). In essence, lasers are sent through the arms, reflected off mirrors at their ends, and then recombined at a photodetector between the two arms. As gravitational waves pass, they stretch spacetime in one direction, causing an interference pattern between the lasers in the two arms. This interference pattern can be measured to understand the character of the wave and, by extension, the event that produced it. However, the precision necessary to detect gravitational waves means any noise can be detrimental to results. The work transitioning from LIGO to aLIGO and current work to improve aLIGO has been focused on reducing noise. The greatest source of noise in aLIGO is quantum noise [5]. One way to decrease quantum fluctuations, however, is to increase the power used: photon shot noise decreases as the number of photons increases (by a factor of $\frac{1}{\sqrt{N}}$).

A multitude of additional optics are added to the interferometer to boost the sensitivity of the system. A power recycling cavity, the arm cavities (Fabry Perot cavities), and a signal recycling cavity form four coupled laser cavities within LIGO for this purpose (Figure 2).
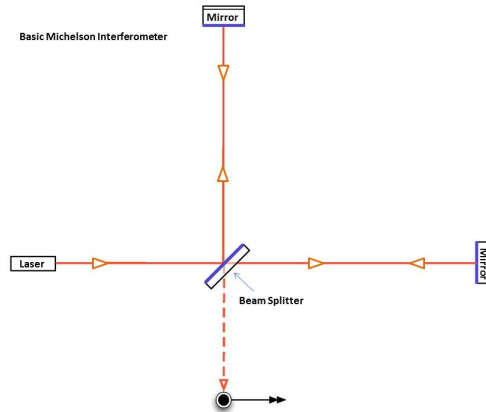
Figure 1: Basic diagram, from the LIGO website [4] showing the Michelson interferometer setup that is the basis of the design of LIGO.

Power recycling mirrors form the first cavity, which allows laser light that has been sent through the system to be reflected back through it, thus "recycling" the laser power. The arm cavities are Fabry Perot cavities, which bounce incoming laser light between two mirrors about 300 times, increasing the distance the light travels and building up the laser light in the system. Finally, the signal recycling mirror forms an anti-resonant optical cavity that extracts only the frequency of light associated with a signal, thus allowing it to be "tuned" to see specific gravitational wave signals.
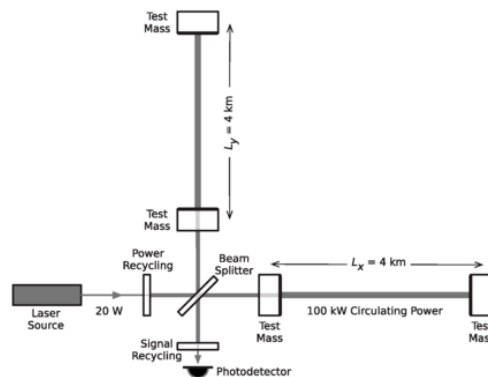

Figure 2: Simplified LIGO diagram showing the Michelson interferometer setup with the power recycling, Fabry Perot, and signal recycling cavities. Modified from Figure 3 in [6]

While these additional optics are imperative to creating a system with enough sensitivity to detect gravitational waves, increasing the power can introduce or amplify other sources of noise or optical losses. One such example is from defects that are physically present in mirrors from their fabrication, particularly point absorber defects [5]. Our project for the summer of 2022 will be to create an in-air facility with a setup to test adaptive optics that counteract these and, ideally, other thermally-induced mirror deformations in aLIGO's mirrors. The key components of the facility include an infrared-detecting camera, a thin

screen to act as a test mass, and the annular ring heater developed by Dr. Richardson and his colleagues [7].

3 Objectives

In order to produce extremely low loss laser cavities, this project seeks to:

1. Construct an in-air optical test facility to allow for the testing of infrared adaptive optics systems.

2. Develop Python code to collect raw data from the infrared sensor in order to test current and future wavefront controlling technology.

4 Methods

4.1 Optical System Setup

The first two weeks of this project were dedicated to setting up the in-air optical table system using a simple triangular optical setup with the ring heater, the IR-absorbing thin screen, and the infrared camera, as in Figure 3. The ring heater, which will have an inner diameter of 0.34 m in its final iteration, will allow for manipulation of the radiation that hits the 0.4 x 0.5 m IR absorbing screen (in place of the 0.34 m test mass in the aLIGO system). The screen, which is 0.1mm thick, is thin enough that the infrared-sensitive camera will be able to detect and map the effects of the ring heater on the test mass based on the image of the back of the screen (the width of the screen is negligible to understanding the infrared pattern).
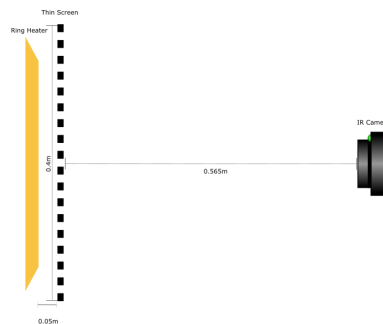

Figure 3: Optical Diagram of the In-Air IR Test Facility Setup

One key component of this system is the infrared camera, which uses microbolometers to detect infrared radiation based on the changing electrical resistance [8]. The microbolometers, sensitive to IR, are arranged in a 640 x 480 array in the camera used for this iteration
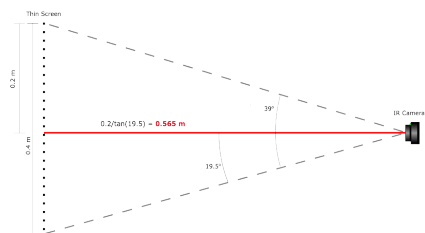
Figure 4: FOV Calculation to Determine Camera Distance from Screen

of the in-air test facility (the Teledyne FLIR A70). Notably, the camera also has a visual camera with a resolution of 1280 x 960 pixels and is used for specific camera modes and it is the field of view of the IR camera that is limiting. The IR camera has a 51° x 39° field of view. In order to allow the camera to capture stray light bouncing off the test mass, 0.4 m, the height of the thin screen, is defined as the desired diameter of the camera's view. Using the vFOV, 39°, the equation $l = \frac{0.4}{2}\tan(\frac{39°}{2})$ yields a distance of 0.565 m. Thus, the camera must be 0.565 m from the screen to contain the entire 0.4m area in it's FOV while still maximizing the FOV (as in Figure 4).
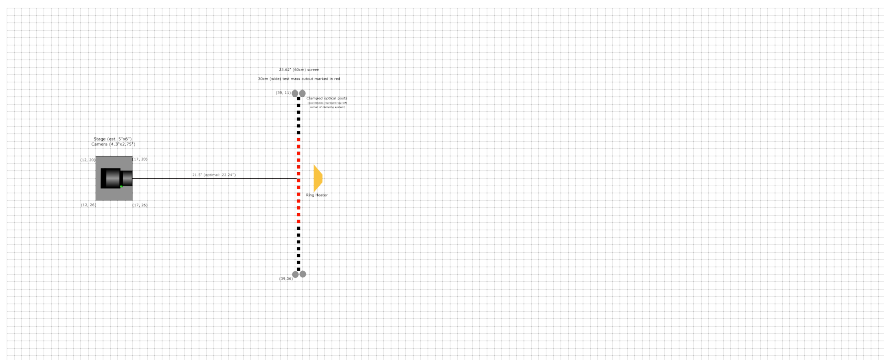

Figure 5: Optical Diagram of the In-Air IR Test Facility Setup Based on the Table Dimensions (1"x1" grid)

Once the correct distances were determined, the table was set up. The table is 4'x10' and the desired optical layout was concentrated on the left side of the table, as in Figure 5. This allows for the most effective use of space and for easier fine adjustment of the camera. The ring heater shown in Figure 5 is a smaller version for proof of concept of the ring heater shown in Figure 3. The ring heater is not yet set up, but the IR-absorbing screen and camera are both mounted (pictured in Figure 6). The IR-absorbing screen was mounted first and has the outline of a test mass painted onto it, allowing the pattern from the ring heater to

be analyzed within the parameters of its use in LIGO.

The camera is mounted on a combination of stages that allows for x, y, z, and rotational fine-tuning. The camera was finely adjusted so that the screen just barely filled the FOV, as predicted in the FOV measurements, by slowly adjusting each degree of freedom.
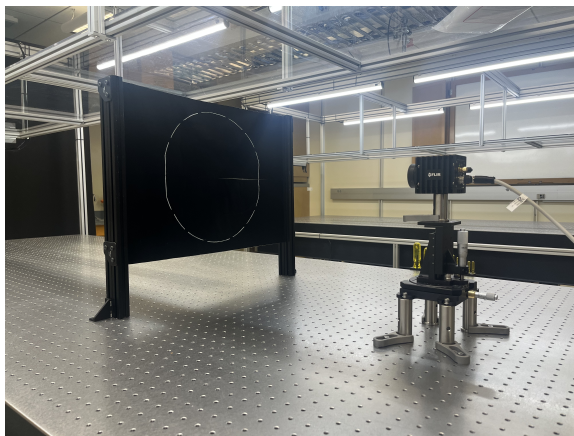

Figure 6: Image of the Table Setup as of July 28

4.2 Controlling the IR Camera

The second portion of this project was to create Python code in order to collect data from the IR camera. Building on the existing API, this code allows for the camera settings to be configured, then collects and displays data characterizing the pattern added to the thin screen by the ring heater.

The current interface created by Python code allows for snapshots of the screen to be taken and for a stream of snapshots to be displayed as live imaging from the camera. When configured to the appropriate settings, which are user inputted values, the images include a color bar that characterizes the temperature of the image, as in Figure 7. Multiple imaging modes are available, including visual, thermal, and various filtered modes.

This code will be used for all upcoming work with this camera with the end goal of using the camera to determine the best heating pattern from the ring in order to mitigate power loss from the point sources in aLIGO's mirrors.

4.2.1 Calculating Temperature

Converting intensity measurements to temperature is a nonlinear, complex process with limited accuracy. However, the FLIR A70 camera has an associated calibration curve that guarantees an error of $\pm 2\%$ within our desired temperature range when object parameters are correctly defined [9]. There are eight object parameters: reflected temperature, atmospheric temperature, object distance, object emissivity. relative humidity, external optics temperature, external optics transmission, and estimated transmission. These parameters work to account for both the radiance of the object being observed, as well as radiation from
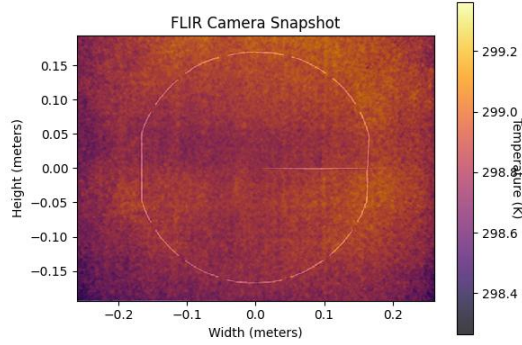
Figure 7: Python Interface When Measuring Temperature

the atmosphere and ambient radiation from nearby objects, as in equation 1. Equation 1 calculates the total incident radiation power based on the radiation power from these three instances. These incident radiation values are acted on by ϵ, the emissivity, and τ, the transmission, as expected by the total radiation law (see Appendix A).

$$W_{tot} = \epsilon\tau W_{obj} + (1 - \epsilon)\tau W_{amb} + (1 - \tau)W_{atm} \tag{1}$$

We can assume the incident radiation power is proportional to the camera signal. Thus, we find the camera signal based only on the incident radiation power from the object itself is represented by Equation 2. The various camera signals can be determined by the object parameters. The process is somewhat lengthy, but a full description is in Appendix B.

$$U_{obj} = \frac{1}{\epsilon\tau}U_{tot} - \frac{1-\epsilon}{\epsilon}U_{amb} - \frac{1-\tau}{\epsilon\tau}U_{atm} \tag{2}$$

To go from this raw input signal to temperature requires two major steps dependent on static camera parameters that FLIR determines for each camera during their calibration process: offset (J_0), gain (J_1), R, B, and F. First, to convert this signal into a raw 16 bit signal, as demanded by the Mono16 pixel format the camera uses, the offset is added to the signal, then the sum is multiplied by the gain. This is set equal to what is known as the RBF function, which is an approximation of Planck's Law commonly used for thermal imaging [10].[1] The result is equation 3.

$$(S + J_0)J_1 = \frac{R}{e^{\frac{B}{T}} - F} \tag{3}$$

This equation can be solved for temperature, yielding equation 4. Notably, the only unknown in this equation is the input signal, S, which we have an expression for from equation 2.

---

[1]For Planck's Law, see Appendix A.

$$T = \frac{B}{ln\left(\frac{R}{(S+J_0)J_1} + F\right)} \tag{4}$$

These expressions were incorporated into the code for the thermal camera image to yield temperature values based on the intensity that the camera measured.[2]

4.2.2   Combining Visual and Thermal Information

One of the main goals of this software was to simultaneously display temperature values and a combination of both visual and thermal images, as exemplified by FLIR's Multi-Spectral Dynamic Imaging, or MSX. MSX overlays details from the visual camera on top of the thermal image from the IR camera to help define the IR image. Unfortunately, the temperature equation identified above (equation 4) is only valid when the camera is acquiring images in the Mono16 pixel format, while MSX only works in the Mono8 pixel format.

To incorporate visual image details into the display, the chosen compromise was to overlay a static visual image of the system on the thermal information. Because the camera is stable and locked in place, the visual image should remain static and thus overlaying a singular visual image should be acceptable. The accuracy of this can be crosschecked by using the overlay in conjunction with the MSX imaging mode and crosschecking their alignment. However, in the case of the system being changed or knocked askew, acquiring a new image is a simple process.

5   Challenges and Next Steps

Currently, the system has a functioning IR camera with code for streaming and taking snapshots. The rest of the project will be spent developing the Python code to collect and characterize the data from the camera's array of microbolometers. The final steps will be to test and refine both the code and the optical table setup.

Once the ring heater and its mounting apparatus are created, the final component of the optical table will be set up. There are no anticipated challenges for this process.

In order to determine the accuracy of the control of the IR camera, the temperature equation should be tested against objects of known temperature value. Additionally, by evaluating the estimated error of each parameter used to calculate temperature, we intend to determine an estimation of the uncertainty of our measured temperature values.

6   Appendix A: Useful Equations

The total radiation law used to determine the coefficients in equation 1, where α refers to incident energy absorption, ρ to reflection, and τ to transmission:

---

[2]The code was largely provided by FLIR's measurement formula [11].

$$W = \alpha W + \rho W + \tau W \tag{5}$$

Planck's Law, from which the RBF function (3) is derived (ν is the electromagnetic radiation frequency):

$$B(\nu, T) = \frac{2h\nu^3}{c^2} \frac{1}{e^{\frac{hc}{k_B T}} - 1} \tag{6}$$

7 Appendix B: Object Parameters

Reflected Energy Parameters:

- Object Emissivity: Based on only the IR-absorptive screen, which has an emissivity of 0.9999 according to manufacturer's specifications.

- Object Distance: calculated based on final placement of aligned camera. In our case, is 0.546m.

- Reflected Temperature: In our case assumed to be the same as the atmospheric temperature, 295K.

Atmospheric Attenuation Parameters:

- Atmospheric Temperature: determined based on the room conditions. In our case, assumed to be 295K.

- Relative Humidity: Determined based on room conditions. In our case, assumed to be 0.5.

- Estimated Transmission: In our case, assumed to be 1.0.

External Optics Parameters:

- External Optics Temperature: In our case, assumed to be 293.15K.

- External Optics Transmission: In our case, assumed to be 1.0.

We recall from equation 2 that in order to determine the radiance resulting from the object's temperature alone (U_{obj}, we need to determine U_{tot}, U_{amb}, and U_{atm}.

U_{tot} is simply the data collected by the camera. The transmission from equation 2 (τ) includes both the transmission from the reflected environment and from the external optics in use. FLIR refers to the measured radiance from the reflected environment, atmosphere and external optics as "pseudo radiance" from the object.

U_{amb} refers to the ambient objects' radiance, which reflects off of the imaged object. This depends on emissivity of the object and the reflected temperature parameter. Using these values, the RBF function (equation 3) can be applied to determine the theoretical signal from the reflected environment.

U_{atm} includes the pseudo radiance of the atmosphere and the pseudo radiance of the external optics, as both rely on the same coefficients. However, the transmission factors (τ) are different in each case, hence there being a separate object parameter for the external optics transmission. As for U_{amb}, these values are calculated using the RBF function (equation 3) to determine the expected signal of the pseudo radiance of the atmosphere and the external optics.

References

[1] Heaviside, Oliver, *A Gravitational and Electromagnetic Analogy.* The Electrician, (1893).

[2] Poincaré, Henri, *Sur la dynamique d' l'électron.* Comptes Rendus of the French Academy of Sciences 140, 1504-1508 (1905).

[3] Einstein, Albert, *Integration Neherunsweise Feldgleichungen der der Gravitation.* Sitzung der phsikalisch-mathematischen Klasse, 688-696 (1916).

[4] https://www.ligo.caltech.edu/page/ligos-ifo

[5] Brooks, A. F., Vajente, G., Yamamoto, H., Abbott, R., Adams, C., Adhikari, R. X., Ananyeva, A., Appert, S., Arai, K., Areeda, J. S., Asali, Y., Aston, S.M., Austin, C., Baer, A. M., Ball, M., Ballmer, S. W., Banagiri, S., Barker, D., Barsotti, L., ... Zweizig, J., *Point Absorbers in Advanced LIGO.* Applied Optics 13, (2021).

[6] Abbott, B. P., Abbott, R., Abbott, T. D., Abernathy, M. R., Acernese, F., Ackley, K., Adams, C., Adams, T., Addesso, P., Adhikari, R. X., Adya, V. B., Affeldt, C., Agathos, M., Agatsuma, K., Aggarwal, N., Aguiar, O. D., Aiello, L., Ain, A., Ajith, P., ... Zweizig, J. *Observation of Gravitational Waves from a Binary Black Hole merger.* Physical Review Letters 116 (2016).

[7] Richardson, Jonathan, *Active Wavefront Control for Megawatt Arm Power.* LVK Meeting, (2022).

[8] https://www.flir.com/products/a50_a70-research-amp-development-kits/?model=89951-0201&vertical=research-and-development-science&segment=solutions

[9] Teledyne FLIR, *FLIR A50/A70 Datasheet.* (2022).

[10] Sundin, Petter, *Intuitive Colorization of Temperature in Thermal Cameras.* 72, (2015).

[11] https://flir.custhelp.com/app/answers/detail/a_id/3321/related/1